



Slab detachment under the Eastern Alps seen by seismic anisotropy



Ehsan Qorbani*, Irene Bianchi, Götz Bokelmann

Department of Meteorology and Geophysics, University of Vienna, Austria

ARTICLE INFO

Article history:

Received 23 July 2014

Received in revised form 17 October 2014

Accepted 21 October 2014

Available online xxx

Editor: P. Shearer

Keywords:

shear-wave splitting
upper mantle dynamics
deformation
lithosphere
asthenospheric flow

ABSTRACT

We analyze seismic anisotropy for the Eastern Alpine region by inspecting shear-wave splitting from SKS and SKKS phases. The Eastern Alpine region is characterized by a breakdown of the clear mountain-chain-parallel fast orientation pattern that has been previously documented for the Western Alps and for the western part of the Eastern Alps. The main interest of this paper is a more detailed analysis of the anisotropic character of the Eastern Alps, and the transition to the Carpathian–Pannonian region. SK(K)S splitting measurements reveal a rather remarkable lateral change in the anisotropy pattern from the west to the east of the Eastern Alps with a transition area at about 12°E. We also model the backazimuthal variation of the measurements by a vertical change of anisotropy. We find that the eastern part of the study area is characterized by the presence of two layers of anisotropy, where the deeper layer has characteristics similar to those of the Central Alps, in particular SW–NE fast orientations of anisotropic axes. We attribute the deeper layer to a detached slab from the European plate. Comparison with tomographic studies of the area indicates that the detached slab might possibly connect with the lithosphere that is still in place to the west of our study area, and may also connect with the slab graveyard to the East, at the depth of the upper mantle transition zone. On the other hand, the upper layer has NW–SE fast orientations coinciding with a low-velocity layer which is found above a more-or-less eastward dipping high-velocity body. The anisotropy of the upper layer shows large-scale NW–SE fast orientation, which is consistent with the presence of asthenospheric flow above the detached slab foundering into the deeper mantle.

© 2014 The Authors. Published by Elsevier B.V. This is an open access article under the CC BY-NC-ND license (<http://creativecommons.org/licenses/by-nc-nd/3.0/>).

1. Introduction

Seismic anisotropy is defined as a directional dependence of seismic velocity. It is assumed that the upper mantle presents significant anisotropy (Maupin and Park, 2007). This anisotropy is most probably due to a non-random distribution of crystallographic orientation of minerals in the olivine-rich ultramafic upper mantle rocks. The non-random distribution is known as lattice-preferred-orientation (LPO). The relation between the typical intrinsic anisotropy in the upper mantle and LPO, which is a result of the deformation, has been well-documented (Babuška and Cara, 1991; Silver and Chan, 1991; Mainprice et al., 2000). It is generally accepted that the anisotropy is due to deformation that either occurred at earlier times (“fossil deformation”) or due to present tectonic activities (Savage, 1999, and references therein). In either case, the anisotropy can indicate the geometry of the flow. Therefore mapping seismic anisotropy can resolve the pattern of

mantle flow in the asthenosphere as well as the fossil deformation pattern within the lithosphere, which has great importance for understanding the upper mantle geodynamics.

The simplest measure of upper mantle anisotropy is the shear-wave splitting, particularly using SKS core phases (e.g. Vinnik et al., 1984; Silver and Chan, 1988; Long and Silver, 2009) which have been studied extensively in recent years. Near-vertical incidence angles of SKS phases give good lateral resolution (i.e. 50 km, the radius of Fresnel zone at 150 km depth), since anisotropy is to be attributed to a steep ray path. However, the depth where the splitting occurs is less well-determined. Although the measuring procedure of shear-wave splitting is straightforward, the practical interpretation of measurements can be quite challenging.

In this study we first present the overall pattern of anisotropy, based on the average values of SKS splitting parameters, then we focus on the spatial changes of the individual measurements and we show striking lateral variations of anisotropy within the region. Later the backazimuthal variation of fast orientations is modeled by means of two anisotropic layers. Finally, using the results of two anisotropic layers modeling, together with some constraints from velocity tomography studies and the analysis of lithospheric

* Correspondence to: 2D506, UZAI, Althanstrasse 14, 1090 Vienna, Austria. Tel.: +43 1 4277 53727.

E-mail address: ehsan.qorbani@univie.ac.at (E. Qorbani).

thickness, we present a possible lithospheric and asthenospheric upper mantle structure for the Eastern Alps.

2. Tectonic setting

The Alps are an arc-shaped double-verging mountain chain developed at the boundary between the Eurasian plate (to the North) and the Adriatic microplate (to the South). They are geographically divided into Southern, Eastern, Central, and Western Alps. Alpine tectonic history is deeply linked to that of the adjacent mountain chains as the Dinarides, the Carpathians and the Apennines. Palaeogeographic reconstructions suggest that in the area where the Alps are located today there was the Meliata Ocean in Triassic time, a marginal ocean basin of the neo-Thetis. In Late Triassic-Early Jurassic this ocean initiated subduction towards SE (Kozur, 1991); in the late Jurassic the opening of the Vardar Ocean took place in its backarc, and at the same time occurred the opening of the Piemont–Ligurian Ocean. During Cretaceous time, another ocean, the Valais, opened on top of the Piemont–Ligurian Ocean, in association with the opening of the Atlantic further to the West (Frisch, 1979; Stampfli, 1994). About 80 Ma ago the Piemont–Ligurian Ocean started subducting below the Adriatic continental margin following the SE directed subduction initiated by Meliata. The contact between the Adriatic continental crust and the Piemont–Ligurian oceanic crust coincide with the geological boundary observed today between the Austroalpine units (in the Eastern Alps) and Penninic Units.

The continental collision between Europe and Adria started ~35 Ma ago (Froitzheim et al., 2008; Handy et al., 2010). The image we have today of the deep structure of the Alps is derived by the interpretation of tomographic images. The different regional models (i.e. Lippitsch et al., 2003; Koulakov et al., 2009; Mitterbauer et al., 2011) agree in identifying two lithospheric roots, one located below the Eastern Alps, and one located below the Central–Western Alps, separated between 12° and 13°E.

On the surface, geodetic data generally agree with a counter-clockwise rotation of the Adriatic plate with respect to stable Europe around a pole in the western Alps (e.g. Calais et al., 2002; Nocquet and Calais, 2004). The CCW rotation of Adria leads to different deformation regimes along the Alpine arc, such as: compression in the Eastern Alps, dextral shear in the Central Alps and transtension or very slow deformation in the western Alps. This suggests that active deformation in the Alps (and in the neighboring Apennines and Dinarides) is controlled, and possibly dynamically driven, by the motion of the Adriatic microplate rather than by the convergence between Africa and Eurasia (Nocquet and Calais, 2003). Vertical GPS ground motions show that the most elevated areas are uplifting while the adjacent sedimentary basins undergo subsidence (Serpelloni et al., 2013). Similar evidence is given by measured erosion rates along the Alpine arc. First of all there is a crucial difference between the European plate (undergoing erosion) and the Adriatic plate (undergoing deposition), suggesting a decoupling between the two plates (Baran et al., 2014). Concerning the European side, the western Alps are characterized by high levels of erosion (>0.6 km/My), while the Eastern Alps show lower erosion rates (~0.06 km/My), with the exception of the Tauern Window area, where a rate of 0.3 km/My is reached (Baran et al., 2014). The difference in erosion rate supports the hypothesis of slab brake-off below the western part of the Alps (von Blanckenburg and Davies, 1995).

3. Data and method

The most frequently used method for constraining the anisotropy within the upper mantle is the shear-wave splitting method,

which is based on birefringence, or splitting of the core shear-waves (SKS) into two orthogonally polarized quasi-phases. The splitting of teleseismic SKS phases has been largely used in order to constrain upper mantle anisotropy (e.g. Vinnik et al., 1984; Silver and Chan, 1991; Margheriti et al., 2003; Buontempo et al., 2008; Barruol et al., 2011). Two fundamental parameters can be measured through this method: the fast orientation azimuth (ϕ , angle between fast axis and radial direction) and the splitting delay between fast and slow polarizations (δt). Assuming that the upper mantle anisotropy is confined in one laterally uniform layer, the horizontal components of SKS phases can be analyzed in order to estimate the amount and symmetry orientations of the azimuthal anisotropy (Vecsey et al., 2008). Several techniques are used to measure splitting parameters. The one used in this study is the transverse component minimization technique (SC) illustrated by Silver and Chan (1991). The application of this technique was performed by the use of the SplitLab package (Wüstefeld et al., 2008).

The splitting parameters are retrieved by applying a grid-search over all possible values of ϕ and δt . The azimuth and delay that better remove the effect of splitting on the T component are those that describe the anisotropic parameters of the mantle beneath the recording station (Wüstefeld et al., 2008). One example of splitting parameters measurement by the SC technique is illustrated in supplementary Figs. S1a, S1b. In most measurements we applied no filter to keep the complete frequency range in order to not lose part of the waveform energy and to prevent the dependence of measured splitting parameters on filtering.

Data collection for this study consisted of the teleseismic events with magnitude M_w greater than 6 occurring in epicentral distance range from 90° to 130° recorded by 33 stations of 5 permanent networks (see Table 1 and Fig. 1). We used data recorded by the Austrian broadband seismological network (OE) between 2002 and 2013. This network includes 12 permanent stations maintained by the Zentralanstalt für Meteorologie und Geodynamik (ZAMG, <http://www.zamg.ac.at>). Data from 13 broadband stations of the Slovenian seismic network (SL) recorded between 2005 and 2013 were included in this study, and accessed through the Observatories and Research Facilities for European Seismology (ORFEUS) database (<http://www.orfeus-eu.org>). Data recorded between 2008 and 2012 were retrieved from one station of the Italian seismic network (IV) maintained by INGV (Istituto Nazionale di Geofisica e Vulcanologia). From the NE-Italian broadband network (NI, operated by OGS, Istituto Nazionale di Oceanografia e di Geofisica Sperimentale), events occurred between 2010 and 2011 recorded by at least two stations have been included. Events occurring between 2006 and 2011 and recorded by 5 stations of the South-Tyrol network (SI) have been included. Altogether 5845 SKS/SKKS phases recorded at all stations have been visually selected. Among these phases, we observed and measured the individual splitting parameters for 868 SKS/SKKS phases. All measurements were classified as “good”, “fair”, and “poor” splitting quality (Barruol et al., 1997; Wüstefeld and Bokelmann, 2007). When no significant energy on transverse components was recorded, the event was considered as displaying a “Null” orientation. 642 Null measurements were observed; out of this number of Nulls, we labeled 372 Null measurements as “good Null”. Supplementary Fig. S1c shows an example of good Null measures.

4. Results

4.1. Splitting parameters; average values

Among 868 measured splitting parameter pairs (fast orientation and splitting delay) showing clear splitting of SKS phases, we selected 470 individual good quality pairs (supplementary Table S2). The calculated average value for each station over the good

Table 1
List of stations and networks used in the study as well as average fast orientations and splitting delays including their corresponding error. Number of splitting measurements (SM) and good quality splitting (GS) are listed together with the number of Null measurements (NM) and good quality Nulls (GN). See Appendix A for Nulls.

Station	Net	Lon (°E)	Lat (°N)	ϕ (°)	ϕ -error	δt (s)	δt -error	SM	GS	NM	GN
ABTA	OE	12.5123	46.7474	85	11	1.26	0.28	17	9	12	7
ARSA	OE	15.5230	47.2505	110	14	1.27	0.19	66	13	87	49
CONA	OE	15.8618	47.9282	118	10	1.01	0.14	42	15	34	15
DAVA	OE	09.8803	47.2867	56	5	1.35	0.11	36	20	33	25
FETA	OE	10.7291	47.0211	63	12	0.97	0.15	26	10	47	21
KBA	OE	13.3447	47.0784	92	10	1.11	0.15	27	16	22	14
MOA	OE	14.2659	47.8495	108	4	1.12	0.13	59	35	56	29
MYKA	OE	13.6416	46.6299	98	6	1.38	0.17	47	31	9	6
OBKA	OE	14.5489	46.5092	118	4	1.47	0.12	85	47	16	11
RETA	OE	10.7623	47.4871	50	6	0.82	0.10	19	13	25	13
SOKA	OE	15.0327	46.6780	122	5	1.16	0.14	33	23	15	7
WTTA	OE	11.6363	47.2638	68	7	1.55	0.27	28	11	61	25
CADS	SL	13.7370	46.2280	74	–	1.20	–	12	1	12	10
CEY	SL	14.4267	45.7388	90	5	1.10	0.13	11	6	22	13
CRES	SL	15.4578	45.8260	125	6	1.05	0.18	32	26	20	14
DOBS	SL	15.4691	46.1495	110	7	1.24	0.16	27	24	3	2
GORS	SL	13.3999	46.3170	108	10	1.38	0.52	12	5	1	1
GROS	SL	15.5017	46.4608	117	6	1.26	0.19	14	10	7	4
JAVS	SL	14.0643	45.8934	92	18	1.09	0.25	22	12	15	13
KNDS	SL	14.3775	45.5276	71	16	0.70	0.32	11	5	17	13
KOGS	SL	16.2503	46.4481	98	4	1.35	0.11	29	22	12	7
LJU	SL	14.5278	46.0438	112	13	1.13	0.21	26	14	20	19
PERS	SL	15.1139	46.6365	124	4	1.05	0.08	28	17	4	3
ROBS	SL	13.5103	46.2450	115	17	1.37	0.29	17	9	4	3
VISS	SL	14.8383	45.8029	112	11	1.65	0.33	9	4	19	13
FVI	IV	12.7804	46.5966	72	7	1.62	0.11	19	11	8	5
CLUD	NI	12.8814	46.4569	82	–	1.90	–	5	1	4	4
ZOU2	NI	12.9729	46.5584	86	10	1.53	0.14	21	11	8	4
ABSI	SI	11.3200	46.7300	52	7	1.59	0.18	14	7	9	4
RISI	SI	12.0800	46.9500	78	12	1.70	0.26	18	16	17	9
ROSI	SI	11.4100	46.9300	63	10	1.75	0.24	26	6	7	1
MOSI	SI	10.5500	46.6200	50	9	0.82	0.12	14	6	11	6
KOSI	SI	11.3800	46.4600	44	4	1.29	0.08	17	14	6	3

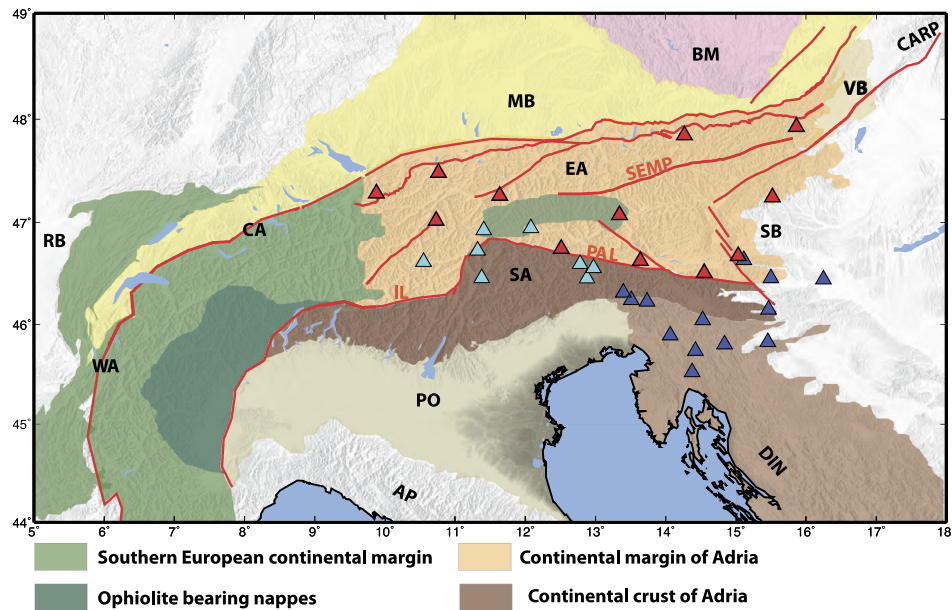


Fig. 1. Map of the study area. Tectonic superunits, as described in the legend, are shown according to their presumed palaeogeographic origin (after Schmid et al., 2004, N. Froitzheim, Geology of the Alps, <http://www.steinmann.uni-bonn.de>). Labels are as in the following: Western Alps (WA), Central Alps (CA), Eastern Alps (EA), Southern Alps (SA), Dinarides (DIN), Apennines (AP), Carpathians (CARP), Bohemian Massif (BM), Vienna Basin (VB), Styria Basin (SB), Molasse Basin (MB), Po Plain (PO), Periadriatic Line (PAL), Insubric Line (IL), Salzach–Ennstal–Mariazell–Puchberg fault (SEMP). Locations of broadband stations used for SKS splitting analysis are shown. Red triangles for the Austrian broadband seismological network (OE); blue triangles for the Slovenian seismic network (SL); cyan for the Italian seismic networks: Istituto Nazionale di Geofisica e Vulcanologia (IV), NE-Italian broadband network (NI), and South-Tyrol network (SI). (For interpretation of the references to color in this figure legend, the reader is referred to the web version of this article.)

measurements is listed in Table 1 as well as the number of total splitting measurements and the number of good splitting measurements. In order to have an estimate of dispersion of individual measurements around the obtained averages, the value of 95% con-

fidence intervals (CI) were calculated. Table 1 shows these values, where ϕ -error corresponds to the circular average fast azimuths, and δt -error to the average splitting delays. ϕ -error is $\leq 13^\circ$ for 29 stations; the largest error value ($\pm 18^\circ$) was obtained for station

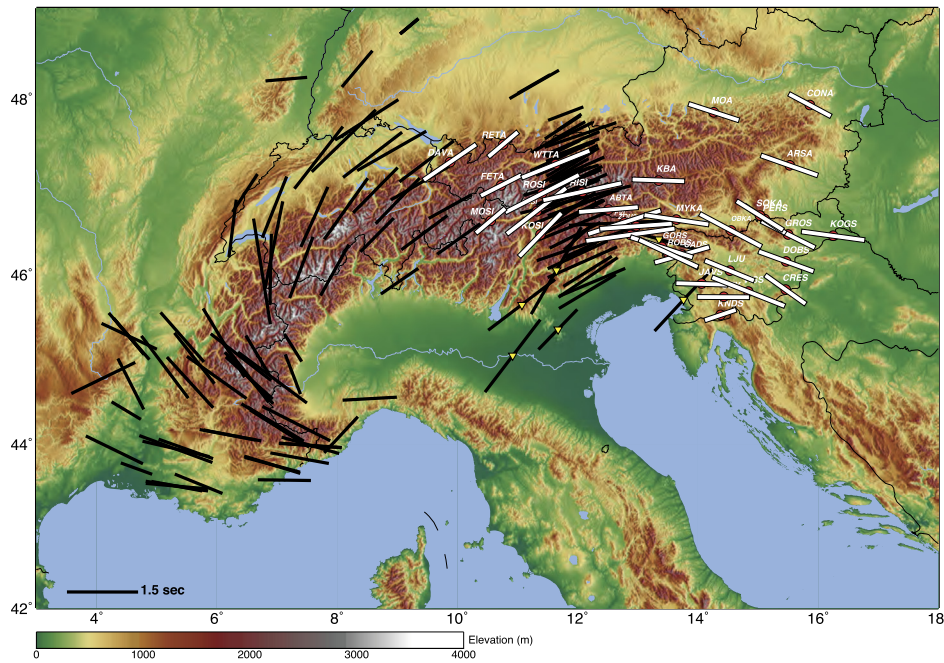


Fig. 2. Map of average SKS splitting parameters calculated over the good quality measurements. Thick white lines represent average fast orientation (ϕ) at each station from this study and Bokelmann et al. (2013). Splitting delays (δt) are shown by the length of the line (see scale on lower left). Black lines display measurements from previous studies (Barruol et al., 2011; Kummerow and Kind, 2006), and stations located in the Southern Alps and Po-plain, marked by triangles, Salimbeni et al. (2013). For discussion see the text. (For interpretation of the colors in this figure, the reader is referred to the web version of this article.)

JAVS. With the exception of KNDS, VISS, and GROS that show 0.32, 0.31, and 0.52 s respectively, the δt -errors are smaller than 0.30 s for all stations. The magnitude of errors indicates that there is a low spread of the individual measurements, so that the average of splitting parameters is a good approximation of overall azimuthal anisotropy beneath the stations and it can be considered and discussed as well for individual splitting measurements.

The average values of splitting pairs are displayed in Fig. 2. The line's orientation presents the average fast orientation azimuth for each station and the line's length indicates the average splitting delay. The stations DAVA, FETA, RETA, WTTA, ABSI, ROSI, MOSI, and KOSI which are located in longitude range between 9°E and 12°E show fast azimuths at about N60° (azimuth from North). These azimuths are in good agreement with the results of previous studies for the Western Alps presented by Barruol et al. (2011) and the Central Alps by Kummerow and Kind (2006) (black lines in Fig. 2). The NE–SW fast orientation detected for the western stations turns gradually to nearly East–West at the stations RISI, ABTA, CLUD, and ZOU2 (located at longitudes between 12°E and 13°E). The station FVI is an exception, with a fast azimuth oriented N72°. East–West fast orientation are detected for station KBA, JAVS and CEY as well (Fig. 2). Further to the East, the fast orientations turn from E–W to NW–SE, where the fast azimuth are predominantly N115° oriented. This is observed for the stations located at longitudes greater than 13°E.

In a previous study (Bokelmann et al., 2013), we described the mountain chain-parallel anisotropy pattern in the upper mantle and discussed the rotation of fast orientation along the Alpine chain. The results of 21 further stations are added to the 12 stations used in that study. They clearly show the rotating pattern of fast orientation along the Alps previously described (seen in Fig. 2). The amounts of average splitting delays are in the reported range by former studies (Barruol et al., 2011; Kummerow and Kind, 2006). The largest splitting delays (larger than 1.0 s) with maximum value of 1.90 s at station CLUD, are observed for the stations located between 13°E and 14°E, southeast of the stations displaying the E–W oriented anisotropic fast azimuth.

4.2. Individual measurements

Assuming that the mantle anisotropy is confined in a single uniform layer with a horizontal symmetry axis, splitting parameters can be averaged among individual measurements retrieved at a single station (Silver and Savage, 1994). Although the average values of fast orientation in this study have provided a reliable estimation for the overall anisotropic structures, the individual splitting parameters should be taken into account, allowing to inspect their variation in more detail. Among all measurements showing clear splitting, 470 were qualified as good in addition to 338 fair and 60 poor qualities.

Fig. 3 shows the good quality individual measurements. Individual fast azimuths at single stations, particularly for those stations located in the eastern part of the region (east of 12°), are grouped into two categories; therefore they are represented in different color. Fast azimuths displaying an angle smaller than 90° with respect to the North are shown in blue. Measurements obtained from stations situated in the western part of the study area show fast azimuth smaller than 90° from the North. The second category (shown by red lines) displays fast azimuth oriented at an angle greater than 90° from North; these orientations are observed east of 12°E (Fig. 3). Few fast azimuth orientation greater than N90° (from North) are observed at stations located between 12° and 13°E, and by moving to the East the number of such oriented fast azimuths gets noticeably larger. According to the fast azimuth categories, we divide the region East and West of longitude 12°E (dashed line in Fig. 3).

The spatial distribution of individual splitting delays is illustrated in Fig. 4a. Different values are shown in three different colors. The largest values which are greater than 2.2 s, are localized around 12°E, 47°N and further to the southeast direction (orange lines in Fig. 4a). A significant decline in splitting delay values is observed about 11°E longitude, in particular stations RETA, FETA, and MOSI (Fig. 4a) show small values mostly less than 1 s.

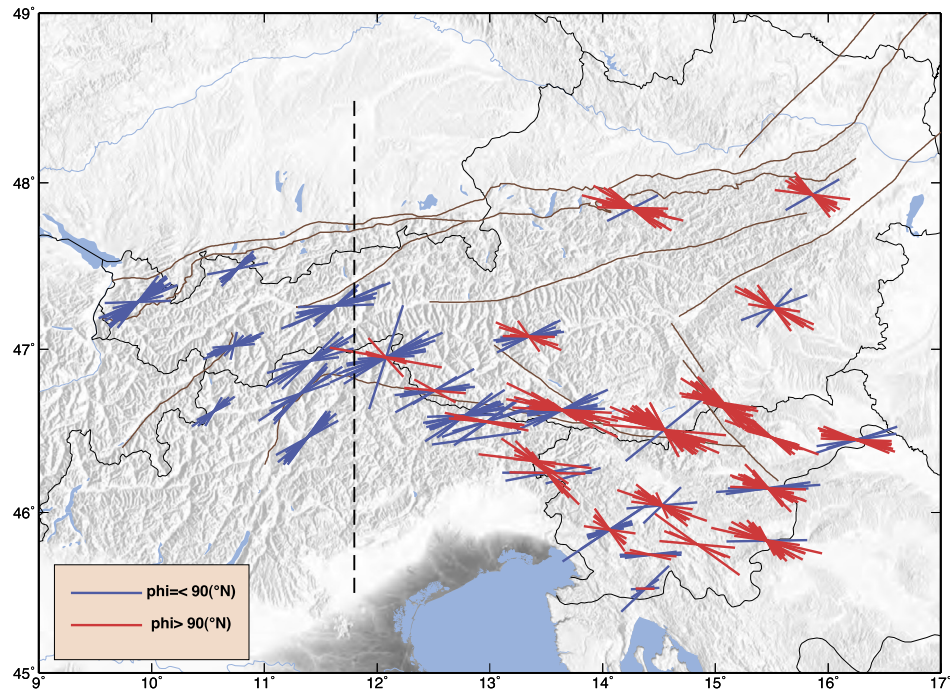


Fig. 3. Good quality individual splitting parameters obtained in this study. The stations show two fast orientation categories (in different colors). Fast axes with azimuths smaller than 90° with respect to North are shown in blue, red for azimuth larger than 90° (mostly obtained for stations located in the eastern part of the study area). The dashed line (at about 12°E) separates the region according to the fast azimuth categories. Brown lines show main tectonic faults (Geological Map of Austria, edited by the Geological Survey of Austria (GBA), 1999, Vienna). (For interpretation of the references to color in this figure legend, the reader is referred to the web version of this article.)

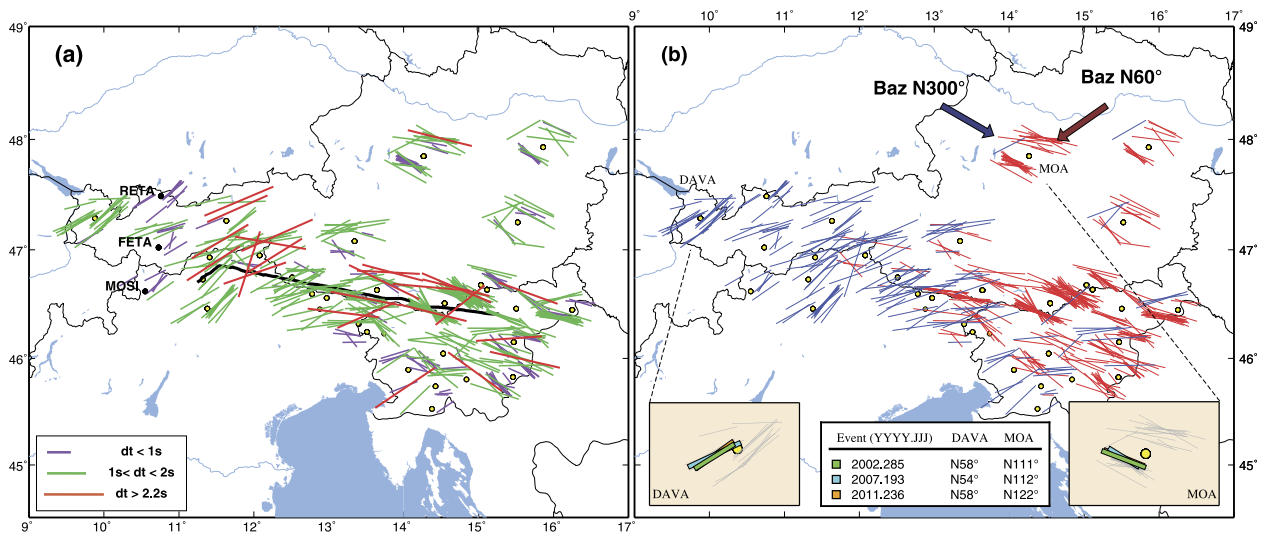


Fig. 4. (a) Individual fast orientations projected along the ray paths down to 150 km depth, colored according to the splitting delay. Largest values (greater than 2.2 s) are observed in the general area along the Periadriatic lineament (black line) and to the south of it. Black circles indicate the three stations that give the smallest splitting delays. (b) Map of backazimuthal variation of measurements. Individual measurements are projected back to 150 km depth. In the eastern part, events from backazimuths around $N60^\circ$ and the opposite direction ($\sim N240^\circ$) show NW–SE fast orientations (red lines). Events from backazimuths around $N300^\circ$ show NE–SW orientations (blue lines). No backazimuthal variation is observed in the western part. Insets represent a zoom of measurements at MOA and DAVA, showing in several examples how the same event can give rise to different fast orientations at different stations. Fast azimuths measured from three events recorded at MOA (in the East) show $N111^\circ$, $N122^\circ$, and $N112^\circ$ while measurements from the same events recorded at DAVA (in the West) show fast azimuths at $N58^\circ$, $N65^\circ$, and $N54^\circ$ (small table). (For interpretation of the references to color in this figure legend, the reader is referred to the web version of this article.)

5. Discussion

5.1. Lateral change of anisotropy

Since every individual measure is obtained from a single event, the variation of splitting parameters can be evaluated as: (i) variation in measured values from one teleseismic event recorded at nearby stations which refers to lateral change of anisotropy in the scale of distance between the stations, (ii) variation in measure-

ments derived from events of different backazimuth at a single station (Margheriti et al., 2003).

In our results, the individual splitting parameters from a single event, recorded at nearby stations, do not show systematic differences. Instead, the single events that show NE–SW fast orientation at the stations in the West, present NW–SE orientation at the stations in the east. Fig. 4b shows examples of different fast azimuth obtained from same events. For instance, a single event (2002.285) recorded at MOA (in the East) exposes a fast azimuth of $N111^\circ$

which is different from fast azimuth $N58^\circ$, recorded at DAVA (in the West). Although, stations do not show local variations, observing two categories of anisotropy pattern in the eastern and western part (Fig. 3), and also considering the variation of anisotropy from singular events (Fig. 4b) indicates a lateral variation of anisotropy, which is remarkable in a larger scale, extending from the Central to the Eastern Alps. Regarding this lateral change, we can consider a transition area in between (at about longitude of 12°E), where the dominant fast orientation changes. Along the Alpine belt, the average fast azimuths follow the mountain belt trend (Barruol et al. (2011) for the western arc; Kummerow and Kind (2006) along the TRANSALP profile in the Central Alps) and show a clear rotating pattern (Bokelmann et al., 2013) for the Central and Eastern Alps (Fig. 2). The mentioned area of transition from individual measurements coincides with the location of the pattern change in average fast azimuth.

The good coverage of event backazimuths from $N38^\circ$ to $N312^\circ$ provides the possibility of assessing the variation of measurements with respect to event backazimuth. We projected all good measurements from their station locations down to 150 km depth, following the ray paths of the SK(K)S phases. Fig. 4b shows the projection of fast orientations. There is no evidence of backazimuthal dependence in the western part of the study area, meaning that events coming from different backazimuth show the same anisotropic fast azimuth. On the other hand, in the eastern part of the region, fast orientation azimuth varies with event backazimuth. In this area, NE–SW fast orientations (shown in blue in Fig. 4b), are mostly obtained from events with backazimuth of around $N300^\circ$; events arriving from backazimuth about $N60^\circ$ and the opposite direction, give NW–SE fast orientation (e.g. station MOA in Fig. 4b). This backazimuthal variation shows that there is clearly a lateral change of anisotropy.

However, the backazimuthal change can sometimes be related to vertical changes of anisotropy, e.g., multi-layer anisotropy or non-horizontal anisotropic layers.

5.2. Vertical changes; modeling of two anisotropic layers

The shear-wave splitting method is performed by assuming the ray passing through an anisotropic medium with a hexagonal and horizontal symmetry axis. Splitting parameters, found under this simplified anisotropic single layer assumption and called apparent measurements, are supposed to be independent of initial polarization orientation (events' backazimuth for the SKS phases) (Silver and Savage, 1994). Observing any backazimuthal dependence in splitting parameters indicates that this single horizontal (hexagonal symmetry) is a simplistic assumption to characterize the anisotropy.

Backazimuthal variations might reveal the depth-dependence of anisotropy (Silver and Savage, 1994; Faccenna et al., 2014). This can be due to the effect of dipping symmetry axis on incoming rays thus showing 2π periodicity of splitting parameters as function of events' backazimuth (Silver and Savage, 1994). In another circumstance, the backazimuthal dependence can be an indicator that incoming shear-waves have been split more than once, which happens in the presence of multiple anisotropic layers. In such case, exposing $\pi/2$ periodicity of measurements in backazimuth suggests the presence of two anisotropic layers (Silver and Savage, 1994; Rümpker et al., 1999). With this intention, the periodicity of measurements was checked at the eastern and western stations separately, as shown in Fig. 5. Single stations located in the eastern part (Fig. 5) present $\pi/2$ periodicity as a function of backazimuth (supplementary Figs. S3, S4). An example (MYKA) in Fig. 5 clearly displays the $\pi/2$ periodicity at a single station. On the other hand, measurements obtained in the West (e.g. WTTA, Fig. 5) do not show this periodicity. The same $\pi/2$ periodicity is

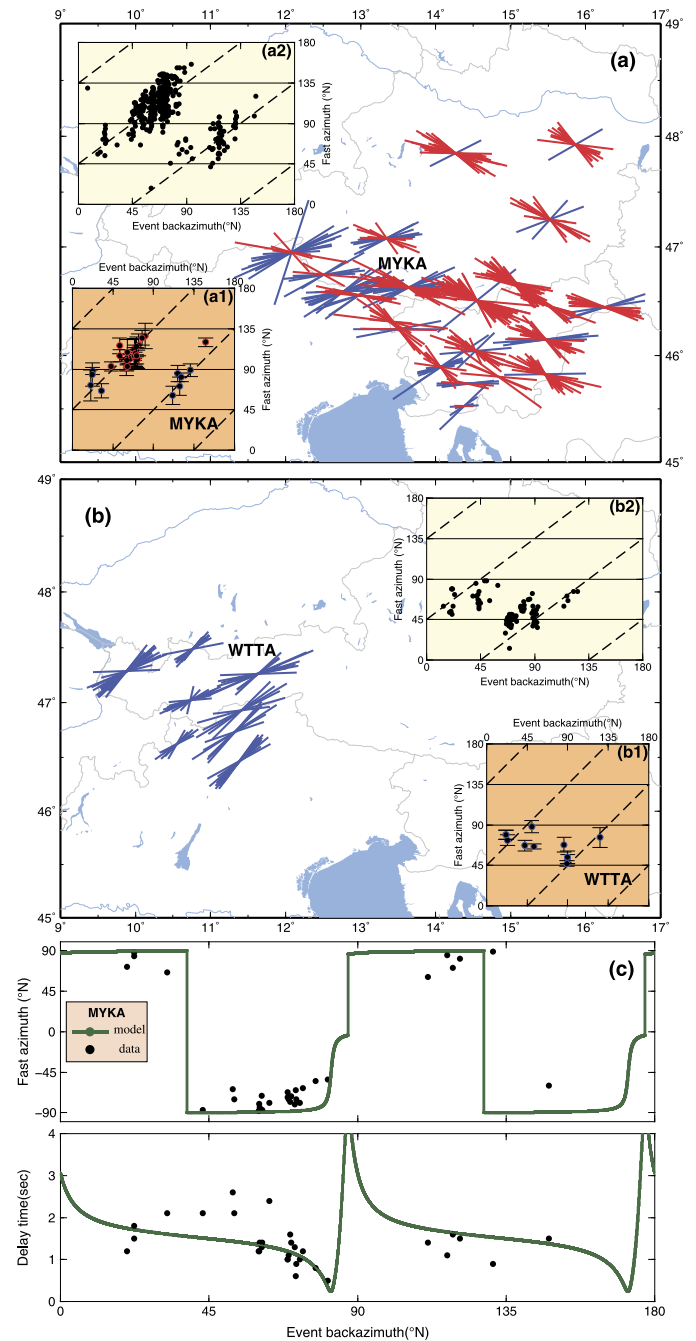


Fig. 5. Periodicity of fast orientations as function of event backazimuth. (a) Measurements shown at the stations in the eastern part. (a1) A single station as example, MYKA, of $\pi/2$ periodicity. (a2) All measurements obtained at stations in the eastern part of the study area, showing $\pi/2$ periodicity. (b) Measurements obtained from the stations in the West do not show $\pi/2$ periodicity neither at the single station (b1, WTTA) nor for all measurements in this area (b2). (c) Theoretical distribution of apparent splitting parameters from the best-fit two layers model for MYKA. Black circles are the good quality measurements used in the modeling process. Top and bottom panel show fast axis orientation and delay time respectively.

recognized for all measurements obtained in eastern part the region (Fig. 5) whereas this is not the case for the stations in the West (Fig. 5).

Observed $\pi/2$ backazimuthal periodicity suggests the presence of two anisotropic layers in the eastern part of the study region. In order to model the two layers, we used the expression between splitting parameters of two anisotropic layers and measurements (apparent parameters), proposed by Silver and Savage (1994):

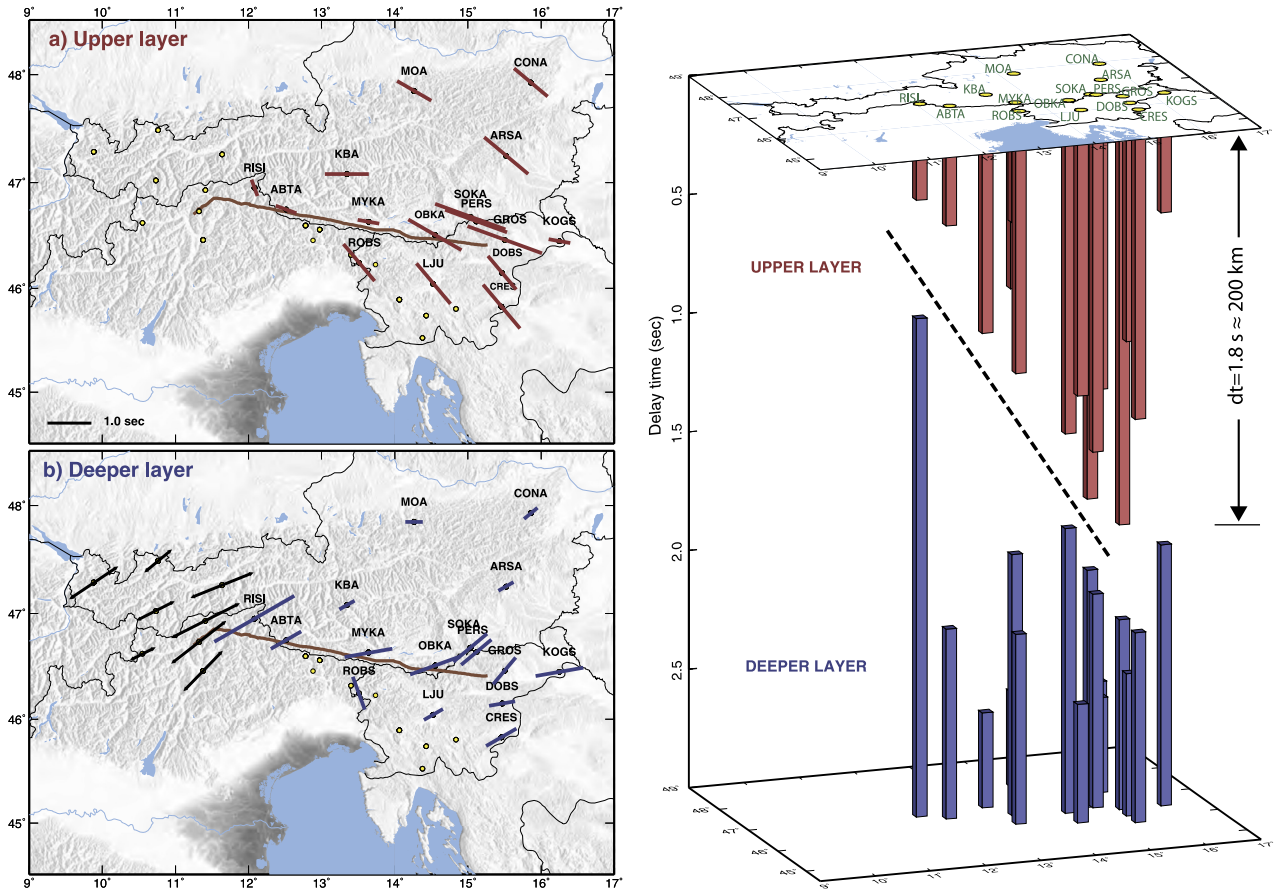


Fig. 6. Left panels: Maps of splitting parameters for the two anisotropic layers. (a) Fast axis azimuths of the upper layer are shown by the orientation of the red lines, with lengths of lines showing the relevant splitting delays. (b) Deeper layer (blue lines). Station location is shown in the horizontal plane. Vertical axes display the amount of splitting delays. Dashed line marks the possibility of an inclined interface between the upper and deeper anisotropic layers. Considering anisotropy magnitude of 3–5% and 1.8 s splitting delay, result in an anisotropic path (layer thickness) of about 200 km at stations GROS and SOKA (right panel, and Fig. 2). The anisotropic path can be estimated using $D = \frac{v_s^2 dt}{dv} = \frac{v_s dt}{\delta v}$, where v_s is shear-wave velocity, $\delta v = \frac{dv}{v}$ represents the magnitude of anisotropy, and dt is the amount of delay time. (For interpretation of the references to color in this figure legend, the reader is referred to the web version of this article.)

$$\tan(\alpha_a) = \frac{a_{p\perp}^2 + C_s^2}{a_{p\perp} a_p + C_s C_c}$$

$$\tan(\theta_a) = \frac{a_{p\perp}}{C_s \cos(\alpha_a) - C_c \sin(\alpha_a)} = \frac{C_s}{a_p \sin(\alpha_a) - a_{p\perp} \cos(\alpha_a)}$$

$$a_p = \cos \theta_1 \cos \theta_2 - \sin \theta_1 \sin \theta_2 \cos(\alpha_2 - \alpha_1),$$

$$a_{p\perp} = -\sin \theta_1 \sin \theta_2 \sin(\alpha_2 - \alpha_1),$$

$$C_c = \cos \theta_1 \sin \theta_2 \cos \alpha_2 + \cos \theta_2 \sin \theta_1 \cos \alpha_1,$$

$$C_s = \cos \theta_1 \sin \theta_2 \sin \alpha_2 + \cos \theta_2 \sin \theta_1 \sin \alpha_1$$

where, α_1 and α_2 are obtained from the difference between fast azimuth of upper/deeper layer and initial polarization (events backazimuth), and multiplied by 2. θ_1 and θ_2 are splitting delays of the two layers multiplied by the angular frequency (0.628 Rad/s) and divided by 2.

All possible models with fast orientations between 0 and N180° (at 10° interval) and splitting delay of 0–4 s (at 0.1 s interval) were created, which gave a total of 518400 models for each station. We also tested the presence of two anisotropic layers by multi-station modeling. In this approach, all good-quality measurements of the stations showing $\pi/2$ periodicity were used in that modeling. However, we observed a poor model fit which was unacceptable in comparison with the results of the single-station approach. This can be due to the effect of the strong lateral change of anisotropy in the eastern Alps since multi-station modeling re-

quires an assumption of no lateral variation. Therefore, the modeling process was individually performed for single stations. Minimization of the Chi-Square value has been used to calculate the fit to the model. The best fitting splitting parameters (ϕ -top, δt -top, ϕ -bot, and δt -bot) for upper and deeper anisotropic layers were chosen according to the minimum Chi-Sq. Coefficient of determination (adjusted R-square) was calculated at each station in order to quantify the quality of the best-fit models (Walker et al., 2005; Fontaine et al., 2007). Adjusted R-square takes the values between $-\infty$ and 1. A two-layer model fits better than a one-layer model, giving values closer to 1 (see Appendix B). The two layers modeling results including the adjusted R-square values are summarized in Table S1. Anisotropic parameters of the upper layer (ϕ -top, δt -top) and deeper layer (ϕ -bot, and δt -bot) are presented for the stations involved in the modeling process.

As shown in Fig. 6a, for the upper layer, most of the stations yield fast axes in NW–SE orientation. They are in agreement with the average fast azimuth of stations in the eastern part (Fig. 2). The results indicate fast azimuths between N110° and N140° with the exception of KBA (90°) and RISI (160°). Moving to the East, the splitting delays for the upper anisotropic layer increase, reaching maximum values (1.7, 1.8 s) at SOKA and GROS respectively (KOGS marks an exception to this trend). The minimum splitting delay (0.4 s) is obtained for RISI which is situated at about 12°E.

Although the fast orientations for the deeper layer are not as tightly grouped as those for the upper layer, the overall pattern of

modeled fast azimuth is in good agreement with the average measured values at the westernmost stations (black lines in Fig. 6b). Stations located North of the Periadriatic lineament generally show similar fast azimuth (exception for MOA). On the other hand, stations in the Southern Alps (south of Periadriatic line) show a complicated pattern. This might indicate complex anisotropic structure in the southern part of the area. Splitting delays show a slight decrease towards the North and towards the South with respect to the Periadriatic lineament, we anyway do not consider meaningful the splitting delays variation for this deeper layer.

Fig. 6 (right panel) shows the three-dimensional spatial distribution of splitting delays of the two layers. The location of the stations involved in the modeling process is displayed in the upper horizontal plane. The vertical axes represent the amount of splitting delays for the anisotropic layers. The splitting delay gradient (from West to East) in the upper layer is clearly visible in the 3D spatial distribution. The maximum splitting delay in the deeper layer (2.1 s) is observed at station RISI, this station also displays the minimum splitting delay for the upper layer. In this situation, the strong effect of anisotropy due to the deeper layer might indicate the larger thickness of deeper structure in comparison with the smaller thickness and weak effect of the upper structure. According to the splitting delay distribution in the upper and deeper layer, we can draw an inclined boundary between these two layers as it is displayed by the dashed line in Fig. 6 (right panel), which would mark a wedge-shaped upper anisotropic layer on the top.

5.3. Anisotropy versus tomographic images

Tomographic images of the eastern Alpine mantle highlight the presence of high-velocity bodies interpreted as the cold lithospheric slab (Piromallo and Morelli, 2003; Lippitsch et al., 2003; Koulakov et al., 2009; Mitterbauer et al., 2011). Along the Alps, the high-velocity anomaly nearly follows the trend of the mountain chain and is placed almost vertically. Fig. 7 shows horizontal depth slices of P-wave velocity anomalies at 150, 300, 510 km after Mitterbauer et al. (2011), and at 150, 240, 350 km after Lippitsch et al. (2003). The high-velocity bodies (blue areas in Fig. 7, at 150 km) have been interpreted as southeastward-subduction of European slab in the West, and as northeastward subducting Adriatic slab in the East (Lippitsch et al., 2003; Kissling et al., 2006). In another hypothesis, the two high-velocity bodies in the West and in the East (Fig. 7, at 150 km) have been interpreted and related to nearly vertical southward-subducting European slab (Mitterbauer et al., 2011; Brückl, 2011). In addition to these two regional-scale models, the upper mantle structure of the European–Mediterranean area has also been imaged by tomography from Piromallo and Morelli (2003) and Koulakov et al. (2009). Depth slices through the velocity models of these studies at 150, 300, 500 km are also shown in Fig. 7.

To compare velocity anomalies and the anisotropy pattern retrieved in this study, the depth projections of individual measurements are superimposed on the tomography sections at 150 km for all models as shown in Fig. 7. The NE–SW fast orientation at longitudes less than $\sim 12^\circ\text{E}$ cannot be related to the high-velocity anomaly alone (cold lithospheric slab) since we observed the same fast orientation outside of the high-velocity body. For the measurements in the eastern part, there is no considerable match of fast orientation neither with the high-velocity nor to the low-velocity anomalies.

Although we cannot directly attribute the anisotropy pattern to the high/low-velocity anomalies, we instead focus on the trend of high-velocity body in comparison to the results of the two anisotropic layers modeling (Fig. 6). In both Lippitsch et al. (2003) and Mitterbauer et al. (2011) models, further at depth, the high-velocity anomalies move ENE-ward to Eastward, revealing a

steeply down-going cold slab, with tendency to follow the Alps–Carpathian trend. This down-going body is observed in Lippitsch et al. (2003) velocity model only down to about 250 km depth while in Mitterbauer et al. (2011) model it is reaches 510 km depth.

Piromallo and Morelli (2003) and Koulakov et al. (2009) show similar velocity structures for the upper mantle (Fig. 7) in which the positive velocity anomalies in the Eastern Alps have been observed at 150 km depth and steeply extend down to the East reaching the depth of 500 km. A slab graveyard has been suggested at a depth ≥ 500 km almost covering the whole area beneath the Alpine–Mediterranean region.

5.4. Origin of the anisotropy

The spatial variation of velocity anomalies from tomographic models together with geophysical and petrofabric findings are employed here in order to constrain depth and origin of the two anisotropic layers.

Fig. 8 displays an East–West cross-section through the velocity anomalies from the tomography model of Mitterbauer et al. (2011), together with the location of this profile on the 150 km depth slice (Fig. 8, top). On the E–W cross-section, the steeply eastward-dipping lithosphere, and the area consisting of low-velocity anomaly on the right-hand side of the dipping slab can be seen. The tapered low-velocity zone is reminiscent of the wedge-shaped distribution of splitting delays of the upper layer (Fig. 6). The correspondence of this low-velocity zone with the geometry of the upper layer can be evaluated by tracing the rays, which reach the stations located on the selected E–W profile. Fig. 8 shows the ray paths, plotted according to the relevant events backazimuth and incidence angles. The events recorded at the station located above the low-velocity zone (SOKA) should mostly sample this area of low velocity. On the other side, the events collected at ABTA should mostly sample the high-velocity zone (Fig. 8). Measurements from these two stations are in good agreement with what we expect from the geometry of velocity anomalies. Dominant fast azimuth are NW–SE oriented for SOKA and mostly NE–SW orientation at ABTA (Fig. 8, top), indicating a noticeable difference in anisotropy structure between down-going lithosphere and the low-velocity zone.

In addition, we can also compare with lithospheric thickness estimates in the region to address the origin of anisotropic structure. It has been shown that crustal (lithospheric) thickness decreases from 50 (170–200) km at the eastern end of Tauern Window to 25 (60) km at the easternmost part of the Alps (Ratschbacher et al., 1991; Frisch et al., 1998, and reference therein) along the mountain chain, over a distance of 200 km. This is in agreement with the lithosphere–asthenosphere boundary (LAB) depth derived by receiver function analysis, which is mostly less than 100 km with an average of 70 km for the Eastern Alps (Bianchi et al., 2014; Jones et al., 2010, and reference therein). For instance, the LAB depth is estimated 98 km at ABTA and 70 km at SOKA (Bianchi et al., 2014). Therefore, the negative gradient of lithospheric thickness toward the East displays an opposite trend with respect to the positive gradient of splitting delays of the upper anisotropic layer (Fig. 6).

Moreover, experimental mineral physics findings derived from upper mantle rock samples suggest an anisotropy of 3–5% in the mantle (Ben Ismail and Mainprice, 1998; Mainprice et al., 2000; Barruol et al., 2011). Taking this magnitude into consideration and the amount of splitting delays of the upper layer, an anisotropic structure ~ 50 km thick (at RISI) and ~ 200 km (at GROS, Fig. 6) is required for the western and eastern end of the upper layer respectively. Consequently, based on crustal and LAB depths under the Eastern Alps, the lithospheric mantle is not thick enough to represent the observed upper anisotropic layer.

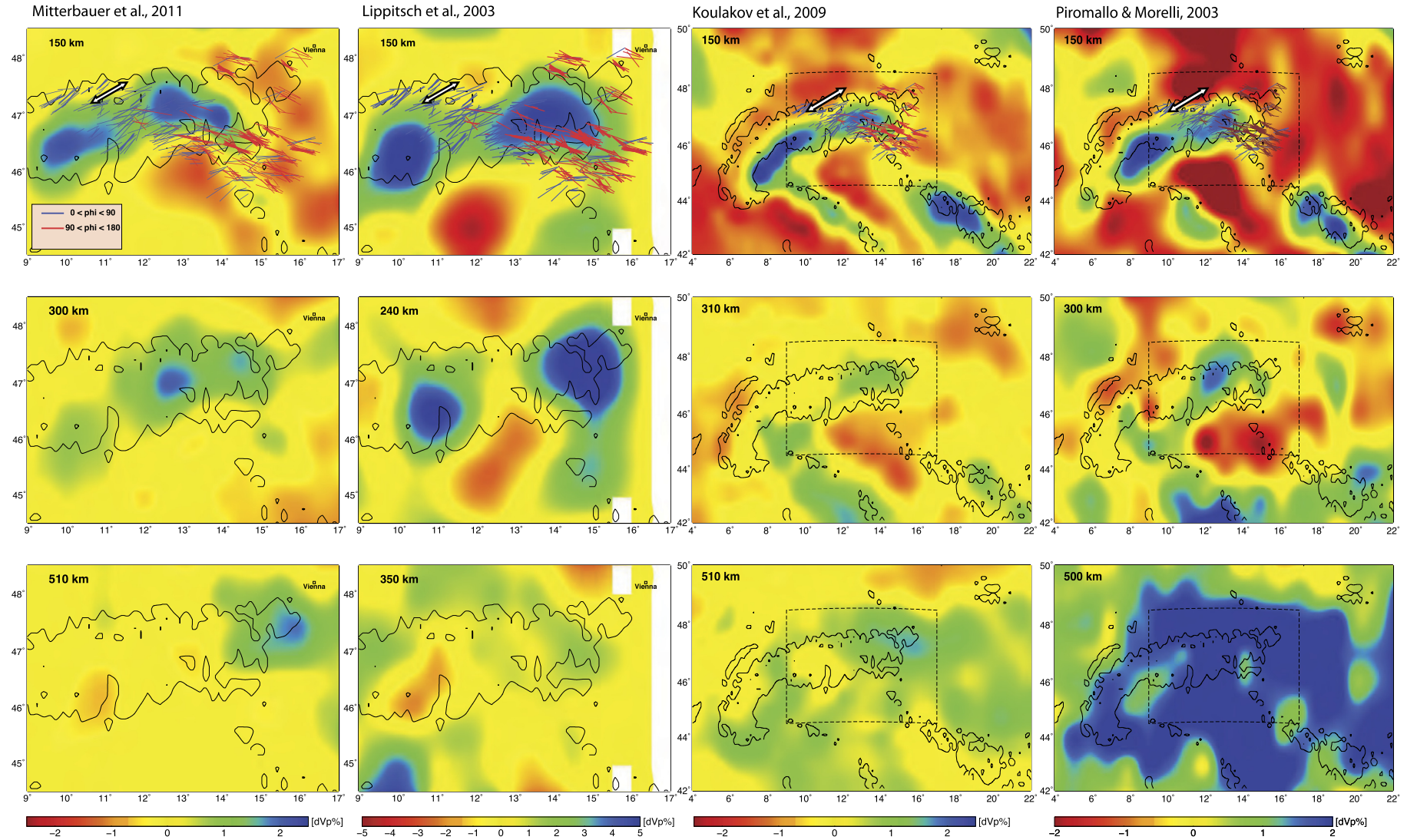


Fig. 7. Tomographic depth slices after Mitterbauer et al. (2011), at 150, 300, and 510 km depth, Lippitsch et al. (2003) at 150, 240, and 350 km, after Koulakov et al. (2009), at 150, 310, and 510 km, and Piromallo and Morelli (2003) at 150, 300, and 500 km depth. Projections at 150 km depth of individual splitting measurements are superimposed on the tomography depth slices for all models. EU plate motion (N240°) with respect to hotspot reference frame (HS3-NUVEL-1A plate model, Gripp and Gordon (2002)), is shown by black–white double arrow. Black contours are topography in 700 m elevation showing the trend of orogenic belts. Coincidence of the trend of Alpine and Dinaride mountain chains with the high-velocity anomalies can be seen at 150 km depth slices. For comparison, the box used in the two models on the left is reproduced on the right panels. (For interpretation of the colors in this figure, the reader is referred to the web version of this article.)

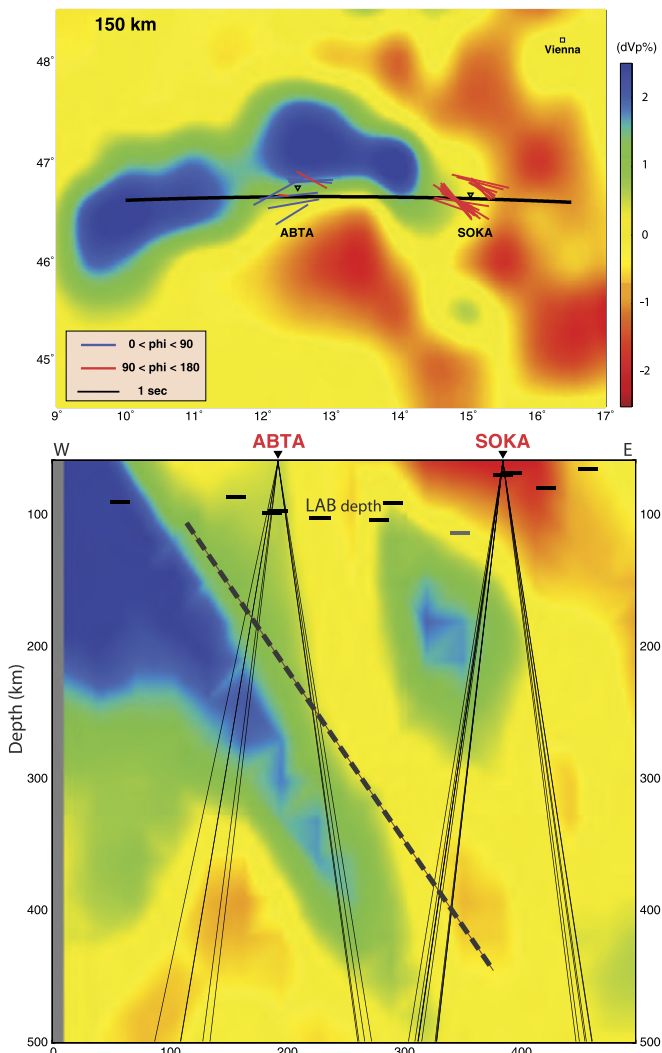


Fig. 8. Horizontal and vertical cross-sections through the velocity anomalies of Mitterbauer et al. (2011). Top: Depth slice (horizontal) at 150 km depth. Projected measurements at ABTA and SOKA together with the station locations are illustrated on the depth slice. Fast axis azimuths measured at ABTA mostly are smaller than $N90^\circ$ (blue lines) while the measurements from SOKA dominantly display NW–SE orientation (red lines). Bottom: E–W cross-section (vertical) through the velocity anomalies. Two stations located above the high-velocity (ABTA) and low-velocity body (SOKA) are shown. Rays coming to these stations are plotted according to their relevant backazimuths and incidence angles. Lithosphere–asthenosphere boundary (LAB) from receiver function analysis Bianchi et al. (2014) is shown by thick dashed lines. An inclined interface (dashed line) can be considered between the eastward down-going high-velocity body and low-velocity zone, likewise between the deeper and upper anisotropic layers (Fig. 6). (For interpretation of the references to color in this figure legend, the reader is referred to the web version of this article.)

Beside that argument, the results of recent shear-wave-splitting analyses (Stuart et al., 2007; Qorbani et al., 2014) showed that the NW–SE fast anisotropic orientation is not restricted to beneath the Eastern Alps only, but is also widely observed within the Carpathian–Pannonian region. This anisotropy pattern spreads in a wide area from the western margin of the Eastern Alps ($\sim 12^\circ\text{E}$) to the easternmost part of the Pannonian basin ($\sim 23^\circ\text{E}$). Over these areas, the rigid lithosphere might have undergone different tectonic events, which has led to changes in the fossil anisotropy within the lithosphere. It is thus unlikely that the anisotropy has the same lithospheric-origin over a distance of 1300 km. Hence, an asthenospheric origin is most probable.

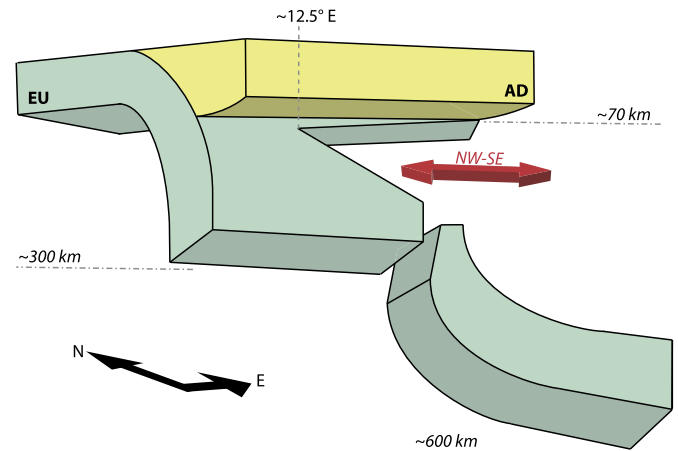


Fig. 9. Schematic figure of the upper mantle structures of the Eastern Alps based on the presence of two layers of anisotropy. The deeper layer with NE–SW fast orientations of anisotropic axes is interpreted as a detached slab of European origin which may connect with the lithosphere under the western part of the Eastern Alps and possibly to the large-scale slab graveyard beneath the Carpathian–Pannonian region. The upper layer, located between the detached slab at the bottom of the thin lithosphere, with NW–SE fast orientations shows similar geometry with the low-velocity area under the Eastern Alps (Fig. 8). The layer is attributed to the asthenospheric flow above the detached slab with NW–SE orientation.

5.4.1. Upper anisotropic layer

The upper layer exposes an anisotropic pattern that is NW–SE oriented, with a mean fast azimuth of $N118^\circ$. This orientation does not follow the trend of the Alpine mountain chain, which is in contrast to the belt-parallel anisotropy that we expect in such a subduction-associated mountain chain, e.g. the Western Alps. Since also the splitting delay is too large to be explained by the lithosphere alone, as described above, sub-lithospheric materials beneath the thin lithosphere likely cause this anisotropy pattern. Therefore we attribute the upper anisotropic layer to an asthenospheric flow, which is oriented NW–SE (Fig. 9).

5.4.2. Deeper anisotropic layer

The deeper layer with anisotropic fast orientation of SW–NE (overall azimuth $N75^\circ$) is in good agreement with the anisotropy detected under the Central Alps (Figs. 2 and 6). We relate the deeper anisotropic layer to a lithospheric origin as a detached slab beneath the Eastern Alps (Fig. 9). This anisotropy is remarkably similar to the anisotropy pattern of the Central Alps, which follows the Alpine chain. The deeper anisotropic layer may thus represent the same lithospheric layer found in the West and Central Alps therefore we suggest a detached slab is originated from the European (EU) slab. This can be part of the Alpine–Tethys lithosphere (Penninic ocean) (Mitterbauer et al., 2011; Brückl, 2011).

By considering about 200 km thickness for the upper layer at GROS in addition to 70 km lithospheric thickness, the deeper layer would begin at a depth of about 270 km which is comparable to already proposed detached slab models that place it at more than 300 km depths (Piromallo and Faccenna, 2004). The detached slab may have started to break-off at about 29 Ma (Schmid et al., 2013) and it might still be connected to the EU slab at about 300 km depth. It also may connect to the slab graveyard under the Eastern Alps and the Carpathian–Pannonian region, which has already been observed (Bijwaard et al., 1998; Piromallo and Morelli, 2003; Koulakov et al., 2009).

5.4.3. Western part, 9°E to 12°E

The western portion of the Eastern Alps shows a simpler anisotropy pattern, which was not included in the process of two layers modeling. Further to the West, at the western arc of the Alps there is a good correlation (at large scale) between anisotropy, the

high-velocity zones (tomographic images), Bouguer gravity anomalies, and the topographic feature of the mountains. These might reflect the lithospheric origin of anisotropy (Barruol et al., 2011). However, to explain the large splitting delays in that area, it has been suggested that anisotropy in the Western and Central Alps may be due to asthenospheric flow that turns around the subducting EU lithosphere (Barruol et al., 2011; Salimbeni et al., 2013). Such upper mantle flow around the subducting slab was also suggested in the subduction rollback model (e.g. Funicello et al., 2006; Piromallo and Faccenna, 2004).

Similarly, in the western portion of the Eastern Alps, a deep EU slab can be associated with anisotropy due to stored deformation from past episodes of the tectonic evolution. Mountain-chain-parallel anisotropy in this region is also a signature for a strong contribution of lithospheric fabric. In the area between 9° and 12°E in which ~N60° average fast azimuth is measured, comparison with tomographic images shows that the stations located inside and outside of the high-velocity regions (cold slab) (see Fig. 7) present similar fast orientations. This indicates that SKS rays have sampled both cold lithosphere and the warmer materials around (low-velocity anomalies), suggesting a correlation between frozen-in anisotropy in the lithosphere and asthenospheric flow, which have similar orientation. There is a coherence of upper mantle flow and lithospheric alignments until longitude of 12°E, in which fast azimuths are in the range of N60°–N70° (Fig. 2).

To test the possibility of plate-motion-related flow, we consider the direction of plate motion. For the European plate it is in a direction of N240° with respect to the hotspot reference frame (HS3-NUVEL-1A plate model, Gripp and Gordon (2002)). This motion may be associated very well to upper mantle flow (e.g. Barruol et al., 2011). Since the fast axis azimuth in the Central Alps is NE–SW oriented, there is a good fit with the plate motion direction and orientation of the anisotropy.

Therefore, in addition to a lithospheric origin for the western portion of the Eastern Alps, we attribute the anisotropy also to asthenospheric flow. This argument is stronger for the northern margin of the mountain chain in which most measurements are located to the North of the high-velocity body (Fig. 7). In the southern margin, although we do not have any measurements to the South of the EU lithospheric slab (high-velocity regions, Fig. 7), the station averages of fast axis azimuth (Salimbeni et al., 2013), show the azimuth of N30° to N53° (Fig. 2) that are close to our results and to the movement direction of EU plate as well. This suggests that part of the observed anisotropy in this region is due to upper mantle flow surrounding the down-going lithospheric slab. However, in this area, it is unclear how much of this anisotropy was caused by past lithospheric deformation and how much by present-day dynamic processes in the asthenosphere.

The schematic Fig. 9 illustrates the suggested interpretation for the Eastern Alps. The attached sub-vertical subduction of the European slab is suggested until about 12°E, in the center of the Tauern Window region. The subducting EU slab starts to detach at about 12°E. The asthenosphere materials thus flow into the wedge-shaped space under the Eastern Alps which extends to the East. The deep detached slab, which might be still connected to the subducting slab, is steeply down-going to reach the slab graveyard under the Eastern Alps and the Carpathian–Pannonian region. The detachment may be caused by the difference in the sinking rates along the subducting plate between deep and shallow part of the slab. This can be due to differences in densities showing different origin of the slabs (e.g. oceanic and continental lithosphere).

The asthenospheric flow above the detached slab is NW–SE oriented. This upper mantle flow might be explained by a corner flow above a subducting slab, with flow direction normal to the strike of the slab (e.g. Fischer et al., 2000), which gives trench-perpendicular anisotropy. However, fluid dynamic model-

ing has shown that the curvature of the slab can impose trench-parallel mantle wedge flow in the arc and trench-perpendicular flow on the flat slab, which is controlled by three-dimensional changes in the slab geometry (Kneller and van Keken, 2007; Hoernle et al., 2008). Such changes from trench-parallel to trench-perpendicular anisotropy also have been suggested by shear-wave splitting observations (Anderson et al., 2004; Kneller and van Keken, 2007).

Although the SKS measurements in the western arc of the Alps show parallelism between anisotropy and the curvature of the slab (Barruol et al., 2011; Bokelmann et al., 2013), the measurements of anisotropy in the Eastern Alps (which is analogous to the flat slab) are oriented at an angle of 30° to 50° with respect to the strike of the EU subducting slab (the North Alpine thrust). The deviation of anisotropy from trench-perpendicular direction might be due to the geometry of the slab detachment in this area where there is a gap between lithosphere on the top and the detached slab on the bottom. The flow may be induced by compensation of the mass lack due to slab detachment in order to fill the gap in between.

6. Conclusions

Upper mantle anisotropic structure under the Eastern Alps has been investigated using SK(K)S splitting measurements. We have shown that while the average values of fast orientations show clear mountain-parallel anisotropy pattern for the Western Alps, this pattern clearly breaks down in the Eastern Alps. Individual measurements at single stations provided an image of lateral changes of anisotropy with a transition area occurring at the same location as the overall pattern is broken. The backazimuthal variations of fast orientations have been modeled as vertical changes in order to assess the depth sources of anisotropy. The results suggest the presence of two anisotropic layers under the Eastern Alps. By analogy between these results and the tomographic images, a possible origin of upper mantle anisotropy is presented as: (1) beneath the Eastern Alps, the deeper layer with NE–SW fast orientation, is characterized by a detached slab of European origin. (2) We attribute the upper layer to the asthenospheric flow with NW–SE orientation which is above the detached slab and below thin lithosphere. The flow can be induced by corner flow at the subduction wedge resulting trench-perpendicular fast orientation pattern. However the deviation of the NW–SE flow orientation from trench-normal direction may possibly be due to variation in the slab geometry which causes the slab detachment. (3) The measurements at the western part of the Eastern Alps show a simple pattern of anisotropy with NE–SW fast orientation, similar to the pattern of the deeper layer. In this area, the lithospheric alignments and sub-lithospheric material flow are aligned in the same direction.

Acknowledgements

We thank Ewald Brückl, Stefan Schmid, Peter Molnar, Walter Kurz, and Wolfgang Frisch for discussions. We also thank Regina Lippitsch, Ulrike Mitterbauer, Ivan Koulakov, Claudia Piromallo and Andrea Morelli for their regional velocity models. The data in this study are from the permanent Austrian network run by the Zentralanstalt für Meteorologie und Geodynamik (ZAMG) (<http://www.zamg.ac.at>), the Slovenian seismic network (SL), the Italian seismic network (IV), the NE-Italian broadband network (NI), and the South-Tyrolian network (SI). We acknowledge funding by the Austrian Science Fund (FWF) through project number 26391.

Appendix A. Null measurements

In the process of attempting to optimize the splitting parameters by minimizing the amplitudes on the transverse component,

we sometimes observe no significant energy on it. In this case, a “Null” orientation is defined, and the shear-wave does not split to quasi phases as fast and slow polarizations (Savage, 1999). We can extract useful information by the employment of “Null” measures, in order to determine which fast orientations cause the absence of energy in the transverse component. Null orientations can be retrieved in two cases: first, the SKS ray sampled an isotropic structure while traveling through upper mantle; second, the back-azimuth of the SKS ray is nearly coincident with the fast or with the slow anisotropy orientation, that means that the initial polarization of the ray is parallel (or almost parallel) to one of the anisotropy axes. In this study we recorded 642 Null measurements of which 372 showed a total polarization on their radial plan (no energy on transverse components). In order to explore the Null orientation variations (green lines in supplementary Fig. S2) in more detail, we use group-averages of individual measures, which are calculated over a group of measurements showing resembling fast azimuth for each station (as in the two categories mentioned in the text).

Supplementary Fig. S2 shows the Null orientations together with the group-averages. In a similar fashion as in Fig. 3, the “Null” azimuth displaying (clockwise) an angle smaller and greater than 90° with respect to the North, are plotted in blue and red respectively. Indeed for the western stations one average is displayed, while for the eastern stations two average orientations are shown. As for the fast azimuths we highlighted duplex orientations in most stations placed in the east of longitude 12°E, Null measurements in this area show four small ranges of backazimuths for some stations (e.g. MOA in supplementary Fig. S2 were they are represented by filled and non-filled arrows respectively). This can be related to two fast and two slow anisotropy orientations at these stations. Some stations (i.e. KBA, ARSA, OBKA) give Nulls in two groups of backazimuthal ranges, which can be related to either two fast orientations or single fast and single slow orientations. On the other hand, the stations positioned to the west of 12°E, mainly give one single fast orientation pattern. This group of stations displays Null measurements mostly in agreement with the derived fast azimuths (e.g. DAVA, supplementary Fig. S2). For some stations (e.g. DOBS, ROSI) we could measure only few “good Nulls”.

Appendix B. Chi-square and R-square

Chi-square calculation is utilized to evaluate the goodness of fit between observational and theoretical measurements. It is the sum of the squares of residuals (vertical distance between the observations and calculations) for each parameter. Modeling the presence of two anisotropic layers is a non-linear regression to find the best-fit model that explains the observational measurements. All possible values for two splitting parameters of each layer (4 in total) are tested. The most likely best-fit values are found by minimizing the Chi-square, which is the summation of the Chi-squares of ϕ , δt , each weighted by the error of the observations (Margheriti et al., 2003; Walker et al., 2005; Fontaine et al., 2007; Salimbeni et al., 2013).

$$X^2 = X_{\phi}^2 + X_{\delta t}^2$$

$$\text{where } X_{\phi}^2 = \sum \frac{(\phi_o - \phi_p)^2}{\sigma_{\phi}^2}, \text{ and } X_{\delta t}^2 = \sum \frac{(\delta t_o - \delta t_p)^2}{\sigma_{\delta t}^2}.$$

To address the question How do we know the best-fit two layers model explain better the observations than one layer model? The coefficient of determination (R-square) is a convenient measure that quantifies the quality of the results (Walker et al., 2004).

$$R^2 = 1 - \frac{SSd}{SSo}$$

$$SSd = X^2 = \sum \left[\frac{(\phi_o - \phi_{2layer})^2}{\sigma_{\phi}^2} + \frac{(\delta t_o - \delta t_{2layer})^2}{\sigma_{\delta t}^2} \right],$$

$$SSo = \sum \left[\frac{(\phi_o - \phi_{1layer})^2}{\sigma_{\phi}^2} + \frac{(\delta t_o - \delta t_{1layer})^2}{\sigma_{\delta t}^2} \right]$$

SSd and SSo are the sum of the squares of residuals for two-layer and one-layer model respectively. We measured the “adjusted R-square” values (Walker et al., 2005; Fontaine et al., 2007) for the best-fit model of each station, which are also listed in supplementary Table S1.

$$R_{adjusted}^2 = 1 - \frac{(N-1)(1-R^2)}{(N-k-1)}$$

where N is the number of data (i.e. two times of number of good measurements at each station), and K is the number of parameters (i.e. 4 parameters). The adjusted R-square value is in a range from $-\infty$ to 1. The value closer to 1 indicates that the observational measurements at a given station are a better representative of two layers model beneath this station than a single layer model.

Appendix C. Supplementary material

Supplementary material related to this article can be found online at <http://dx.doi.org/10.1016/j.epsl.2014.10.049>.

References

- Anderson, M.L., Zandt, G., Triep, E., Fouch, M., Beck, S., 2004. Anisotropy and mantle flow in the Chile–Argentina subduction zone from shear wave splitting analysis. *Geophys. Res. Lett.* 31. <http://dx.doi.org/10.1029/2004GL020906>.
- Babuška, V., Cara, M., 1991. *Seismic Anisotropy in the Earth*. Kluwer Academic Publishers Dordrecht, The Netherlands; Boston.
- Baran, R., Friedrich, A.M., Schlunegger, F., 2014. The late Miocene to Holocene erosion pattern of the Alpine foreland basin reflects Eurasian slab unloading beneath the western Alps rather than global climate change. *Lithos* 6, 124–131. <http://dx.doi.org/10.1130/L307.1>.
- Barruol, G., Silver, P., Vauchez, A., 1997. Seismic anisotropy in the eastern United States: deep structure of a complex continental plate. *J. Geophys. Res.* 102, 8329–8348.
- Barruol, G., Bonnin, M., Pedersen, H., Bokelmann, G., Tiberi, C., 2011. Belt-parallel mantle flow beneath a halted continental collision: the western Alps. *Earth Planet. Sci. Lett.* 302, 429–438. <http://dx.doi.org/10.1016/j.epsl.2010.12.040>.
- Ben Ismail, W., Mainprice, D., 1998. An olivine fabric database: an overview of upper mantle fabrics and seismic anisotropy. *Tectonophysics* 296, 145–157. [http://dx.doi.org/10.1016/S0040-1951\(98\)00141-3](http://dx.doi.org/10.1016/S0040-1951(98)00141-3).
- Bianchi, I., Miller, M.S., Bokelmann, G., 2014. Insights on the upper mantle beneath the Eastern Alps. *Earth Planet. Sci. Lett.* 403, 199–209. <http://dx.doi.org/10.1016/j.epsl.2014.06.051>.
- Bijwaard, H., Spakman, W., Engdahl, E.R., 1998. Closing the gap between regional and global travel time tomography. *J. Geophys. Res.* 103, 30055–30078. <http://dx.doi.org/10.1029/98JB02467>.
- Bokelmann, G., Qorbani, E., Bianchi, I., 2013. Seismic anisotropy and large-scale deformation of the Eastern Alps. *Earth Planet. Sci. Lett.* 383, 1–6. <http://dx.doi.org/10.1016/j.epsl.2013.09.019>.
- Brückl, E., 2011. *Lithospheric Structure and Tectonics of the Eastern Alps – Evidence from New Seismic Data*. In: Closson, D. (Ed.), *Tectonics*. ISBN 978-953-307-545-7.
- Buontempo, B., Bokelmann, G., Barruol, G., Moralest, J., 2008. Seismic anisotropy beneath southern Iberia from SKS splitting. *Earth Planet. Sci. Lett.* 273, 237–250.
- Calais, E., Nocquet, J.M., Jouanne, F., Tardy, M., 2002. Current strain regime in the Western Alps from continuous Global Positioning System measurements, 1996–2001. *Geology* 30, 651–654. [http://dx.doi.org/10.1130/0091-7613\(2002\)030-0651:CSRITW-2.0.CO;2](http://dx.doi.org/10.1130/0091-7613(2002)030-0651:CSRITW-2.0.CO;2).
- Faccenna, C., Becker, T.W., Auer, L., Billi, A., Boschi, L., Brun, J.P., Capitanio, F.A., Funicello, F., Horvath, F., Jolivet, L., Piromallo, C., Royden, L., Rossetti, F., Serpelloni, E., 2014. Mantle dynamics in the Mediterranean. *Rev. Geophys.* <http://dx.doi.org/10.1002/2013RG000444>.
- Fischer, K.M., Parmentier, E.M., Stine, A.R., Wolf, E.R., 2000. Modeling anisotropy and plate-driven flow in the Tonga subduction zone back arc. *J. Geophys. Res.* 105, 16181–16191. <http://dx.doi.org/10.1029/1999JB900441>.
- Fontaine, F.R., Barruol, G., Tommasi, A., Bokelmann, G.H.R., 2007. Upper-mantle flow beneath French Polynesia from shear wave splitting. *Geophys. J. Int.* 170, 1262–1288. <http://dx.doi.org/10.1111/j.1365-246X.2007.03475.x>.

- Frisch, W., 1979. Tectonic progradation and plate tectonic evolution of the Alps. *Tectonophysics* 60, 121–139. [http://dx.doi.org/10.1016/0040-1951\(79\)90155-0](http://dx.doi.org/10.1016/0040-1951(79)90155-0).
- Frisch, W., Kuhleman, J., Dunkl, L., Brügel, A., 1998. Palinspastic reconstruction and topographic evolution of the eastern Alps during late tertiary tectonic extrusion. *Tectonophysics* 279, 1–15.
- Froitzheim, N., Plasienska, D., Schuster, R., 2008. Alpine tectonics of the Alps and Western Carpathians. In: McCann, T. (Ed.), *The Geology of Central Europe: Mesozoic and Cenozoic*. Geol. Soc., London, pp. 1141–1232.
- Funiciello, F., Moroni, M., Piromallo, C., Faccenna, C., Cenedese, A., Bui, H.A., 2006. Mapping mantle flow during retreating subduction: laboratory models analyzed by feature tracking. *J. Geophys. Res.* 111. <http://dx.doi.org/10.1029/2005JB003792>.
- Gripp, A.E., Gordon, R.G., 2002. Young tracks of hotspots and current plate velocities. *Geophys. J. Int.* 150, 321–361. <http://dx.doi.org/10.1046/j.1365-246X.2002.01627.x>.
- Handy, M.R., Schmid, S.M., Bousquet, R., Kissling, E., Bernoulli, D., 2010. Reconciling plate-tectonic reconstructions of Alpine Tethys with the geological-geophysical record of spreading and subduction in the Alps. *Earth-Sci. Rev.* 102, 121–158. <http://dx.doi.org/10.1016/j.earscirev.2010.06.002>.
- Hoernle, K., Abt, D.L., Fischer, K.M., Nichols, H., Hauff, F., Abers, G.A., van den Bogaard, P., Heydolph, K., Alvarado, G., Protti, M., Strauch, W., 2008. Arc-parallel flow in the mantle wedge beneath Costa Rica and Nicaragua. *Nature* 451, 1094–1097. <http://dx.doi.org/10.1038/nature06550>.
- Jones, A.G., Plomerova, J., Korja, T., Sodoudi, F., Spakman, W., 2010. Europe from the bottom up: a statistical examination of the central and northern European lithosphere–asthenosphere boundary from comparing seismological and electromagnetic observations. *Lithos* 120, 14–29. <http://dx.doi.org/10.1016/j.lithos.2010.07.013>.
- Kissling, E., Schmid, S.M., Lippitsch, R., Ansonge, J., Fugenschuh, B., 2006. Lithosphere structure and tectonic evolution of the Alpine arc: new evidence from high-resolution teleseismic tomography. *Mem. Geol. Soc. Lond.* 32, 129–145. <http://dx.doi.org/10.1144/GSL.MEM.2006.032.01.08>.
- Kneller, E.A., van Keken, P.E., 2007. Trench-parallel flow and seismic anisotropy in the Mariana and Andean subduction systems. *Nature* 450, 1222–1225. <http://dx.doi.org/10.1038/nature06429>.
- Koulakov, I., Kaban, M.K., Tesauro, M., Cloetingh, S., 2009. P- and S-velocity anomalies in the upper mantle beneath Europe from tomographic inversion of ISC data. *Geophys. J. Int.* 179, 345–366. <http://dx.doi.org/10.1111/j.1365-246X.2009.04279.x>.
- Kozur, H., 1991. The evolution of the Meliata–Hallstatt ocean and its significance for the early evolution of the Eastern Alps and Western Carpathians. *Palaeogeogr. Palaeoclimatol. Palaeoecol.* 87, 109–135. [http://dx.doi.org/10.1016/0031-0182\(91\)90132-B](http://dx.doi.org/10.1016/0031-0182(91)90132-B).
- Kummerow, J., Kind, R., 2006. Shear wave splitting in the Eastern Alps observed at the TRANSALP network. *Tectonophysics* 414, 117–125. <http://dx.doi.org/10.1016/j.tecto.2005.10.023>.
- Lippitsch, R., Kissling, E., Ansonge, J., 2003. Upper mantle structure beneath the Alpine orogen from high-resolution tomography. *J. Geophys. Res.* 108, 2376. <http://dx.doi.org/10.1029/2002JB002016>.
- Long, M., Silver, P., 2009. Shear wave splitting and mantle anisotropy: measurements, interpretations. *Surv. Geophys.* 30, 407–461. <http://dx.doi.org/10.1007/s10712-009-9075-1>.
- Mainprice, D., Barruol, G., Ben Ismail, W., 2000. The seismic anisotropy of the Earth's mantle: from single crystal to polycrystal. In: Karato, S., Forte, A., Liebermann, R., Masters, G., Stixrude, L. (Eds.), *Composition, Structure and Dynamics of the Lithosphere–Asthenosphere System*. In: *Geophys. Monogr.*, vol. 117. AGU, p. 237.
- Margheriti, L., Lucente, F., Pondrelli, S., 2003. SKS splitting measurements in the Apenninic–Tyrrhenian domain (Italy) and their relation with lithospheric subduction and mantle convection. *J. Geophys. Res.* 108, 2218. <http://dx.doi.org/10.1029/2002JB001793>.
- Maupin, V., Park, J., 2007. *Theory and Observations – Wave Propagation in Anisotropic Media*. In: Schubert, G. (Ed.), *Treatise on Geophysics*. Elsevier, Amsterdam, pp. 289–321, Chapter 1.09.
- Mitterbauer, U., Behm, M., Brückl, E., Lippitsch, R., Guterch, A., Keller, G., Koslovskaya, E., 2011. Shape and origin of the East-Alpine slab constrained by the ALPASS teleseismic model. *Tectonophysics* 510, 195–206. <http://dx.doi.org/10.1016/j.tecto.2011.07.001>.
- Nocquet, J.M., Calais, E., 2003. Crustal velocity field of western Europe from permanent GPS array solutions, 1996–2001. *Geophys. J. Int.* 154, 72–88. <http://dx.doi.org/10.1046/j.1365-246X.2003.01935.x>.
- Nocquet, J.M., Calais, E., 2004. Geodetic Measurements of Crustal Deformation in the Western Mediterranean and Europe. *Pure Appl. Geophys.* 161, 661–681. <http://dx.doi.org/10.1007/s00024-003-2468-z>.
- Piromallo, C., Faccenna, C., 2004. How deep can we find the traces of Alpine subduction? *Geophys. Res. Lett.* 31. <http://dx.doi.org/10.1029/2003GL019288>.
- Piromallo, C., Morelli, C., 2003. P wave tomography of the mantle under the Alpine–Mediterranean area. *J. Geophys. Res.* 108, 2065. <http://dx.doi.org/10.1029/2002JB001757>.
- Qorbani, E., Bokelmann, G., Kovács, I., Falus, G., 2014. Anisotropic structure of the Carpathian–Pannonian region: reprocessing SKS splitting data for the CBP project stations. In: *EGU General Assembly 2014*. Vienna, Austria. EGU2014-5166.
- Ratschbacher, L., Frisch, W., Linzer, H.G., Merle, O., 1991. Lateral extrusion in the eastern Alps, part II: Structural analysis. *Tectonics* 10, 257–271. <http://dx.doi.org/10.1029/90TC02623>.
- Rümpker, G., Tommasi, A., Kendall, J.M., 1999. Numerical simulations of depth-dependent anisotropy and frequency-dependent wave propagation effects. *J. Geophys. Res.* 104, 23141–23153. <http://dx.doi.org/10.1029/1999JB900203>.
- Salimbeni, S., Pondrelli, S., Margheriti, L., 2013. Hints on the deformation penetration induced by subductions and collision processes: seismic anisotropy beneath the Adria region (Central Mediterranean). *J. Geophys. Res.* 118, 5814–5826. <http://dx.doi.org/10.1002/2013JB010253>.
- Savage, M., 1999. Seismic anisotropy and mantle deformation: what have we learned from shear wave splitting? *Rev. Geophys.* 37, 65–106.
- Schmid, S., Fugenschuh, B., Kissling, E., Schuster, R., 2004. Tectonic map and overall architecture of the Alpine orogen. *Eclogae Geol. Helv.* 97, 93–117. <http://dx.doi.org/10.1007/s00015-004-1113-x>.
- Schmid, S., Scharf, A., Handy, M., Rosenberg, C., 2013. The Tauern Window (Eastern Alps, Austria): a new tectonic map, with cross-sections and a tectonometamorphic synthesis. *Swiss J. Geosci.* 106, 1–32. <http://dx.doi.org/10.1007/s00015-013-0123-y>.
- Serpelloni, E., Faccenna, C., Spada, G., Dong, D., Williams, S.D.P., 2013. Vertical GPS ground motion rates in the Euro-Mediterranean region: new evidence of velocity gradients at different spatial scales along the Nubia-Eurasia plate boundary. *J. Geophys. Res.* 118, 6003–6024. <http://dx.doi.org/10.1002/2013JB010102>.
- Silver, P.G., Chan, W., 1988. Implications for continental structure and evolution from seismic anisotropy. *Nature* 335, 34–39. <http://dx.doi.org/10.1038/335034a0>.
- Silver, P.G., Chan, W.W., 1991. Shear wave splitting and subcontinental mantle deformation. *J. Geophys. Res.* 96, 16429–16454.
- Silver, P.G., Savage, M.K., 1994. The interpretation of shear-wave splitting parameters in the presence of two anisotropic layers. *Geophys. J. Int.* 119, 949–963. <http://dx.doi.org/10.1111/j.1365-246X.1994.tb04027.x>.
- Stampfli, G., 1994. Exotic terrains in the Alps: a solution for a single Jurassic ocean. *Schweiz. Mineral. Petrogr. Mitt.* 74, 449–452.
- Stuart, G., Houseman, G., Dando, B., Hegedüs, E., Brückl, E., Radovanovic, S., Falus, G., Kovács, I., Hausmann, H., Brisbane, A., 2007. Understanding extension within a convergent orogen: initial results on seismic structure from the Carpathian Basins Project. In: *AGU Fall Meeting 2007*. San Francisco, CA, USA.
- Vecsey, L., Plomerová, J., Babuška, V., 2008. Shear-wave splitting measurements – Problems and solutions. *Tectonophysics* 462, 178–196. <http://dx.doi.org/10.1016/j.tecto.2008.01.021>.
- Vinnik, L., Kosarev, G., Makeeva, L., 1984. Lithosphere anisotropy from the observation of SKS and SKKS waves. *Dokl. Akad. Nauk SSSR* 278, 1335–1339.
- von Blanckenburg, F., Davies, J.H., 1995. Slab breakout: a model for syncollisional magmatism and tectonics in the Alps. *Tectonics* 14, 120–131. <http://dx.doi.org/10.1029/94TC02051>.
- Walker, K.T., Nyblade, A.A., Klemperer, S.L., Bokelmann, G.H.R., Owens, T.J., 2004. On the relationship between extension and anisotropy: constraints from shear wave splitting across the East African Plateau. *J. Geophys. Res.* 109. <http://dx.doi.org/10.1029/2003JB002866>.
- Walker, K.T., Bokelmann, G.H.R., Klemperer, S.L., Bock, G., 2005. Shear-wave splitting around the Eifel hotspot: evidence for a mantle upwelling. *Geophys. J. Int.* 163, 962–980. <http://dx.doi.org/10.1111/j.1365-246X.2005.02636.x>.
- Wüstefeld, A., Bokelmann, G., 2007. Null detection in shear-wave splitting measurements. *Bull. Seismol. Soc. Am.* 97, 1204–1211. <http://dx.doi.org/10.1785/0120060190>.
- Wüstefeld, A., Bokelmann, G., Zaroli, C., Barruol, G., 2008. SplitLab: a shear-wave splitting environment in Matlab. *Comput. Geosci.* 34, 515–528.